

Differential Reynolds Stress Modeling for Aeronautics

René-Daniel Cécora

**Technische Universität Braunschweig, Institute of Fluid Mechanics, Braunschweig, D-38106, Germany*

Bernhard Eisfeld

†*DLR Institute of Aerodynamics and Flow Technology, Braunschweig, D-38108, Germany*

Axel Probst

‡*DLR Institute of Aerodynamics and Flow Technology, Göttingen, D-37073, Germany*

Simone Crippa

§*DLR Institute of Aerodynamics and Flow Technology, Braunschweig, D-38108, Germany*

Rolf Radespiel

¶*Technische Universität Braunschweig, Institute of Fluid Mechanics, Braunschweig, D-38106, Germany*

A comparison of two differential Reynolds stress models for aeronautical flows is presented. The SSG/LRR- ω model combines the Speziale-Sarkar-Gatski (SSG) pressure-strain model with the Launder-Reece-Rodi (LRR) model towards the wall, where the length scale is supplied by Menter's BSL ω -equation. The JHh-v2 model from Jakirlić and Hanjalić has been particularly designed for representing the correct near wall behavior of turbulence and has been adapted to aeronautical needs. Its length scale is provided by a transport equation for the homogeneous part of the dissipation rate.

The models are applied to a series of test cases relevant to aeronautics, showing improved predictions compared to eddy viscosity models particularly in case of separation.

Nomenclature

A	Reynolds stress flatness parameter
A_2, A_3	Reynolds stress anisotropy invariants
\tilde{a}_{ij}	Component of Reynolds stress anisotropy tensor
C	Coefficient of log-law
C_i, C_i^*	Coefficients of SSG model
$\hat{C}, \hat{C}_i, \hat{C}'_1, \hat{C}^w_i$	Coefficients of JHh-v2 model
C_p	Specific heat at constant pressure, $m^2/(s^2 K)$
C_v	Specific heat at constant volume, $m^2/(s^2 K)$
C_μ	Equilibrium parameter
c	Chord length
$c_2^{(LRR)}$	Coefficient of LRR model
c_f	Skin friction coefficient
c_l	Lift coefficient
c_p	Pressure coefficient
D	Reynolds stress diffusion coefficient

*Research Scientist.

†Research Scientist, Dept. C²A²S²E.

‡Research Scientist, Dept. C²A²S²E.

§Research Scientist, Dept. C²A²S²E.

¶Professor.

$D^{(\tilde{k})}$	Diffusion rate of kinetic turbulence energy, m^2/s^3
D_{ij}	Component of specific diffusion tensor, m^2/s^3
$D_{ij}^{(p)}$	Component of specific pressure diffusion tensor, m^2/s^3
$D_{ij}^{(\nu)}$	Component of specific viscous diffusion tensor, m^2/s^3
d	Distance to nearest wall-point, m
E	Specific total energy, m^2/s^2 ; Dissipation flatness parameter
E_2, E_3	Dissipation anisotropy invariants
e	Specific internal energy, m^2/s^2
F_1	Blending function by Menter
f, f_w, f_ε	Damping functions in JHh-v2 model
H	Specific total enthalpy, m^2/s^2
h	Specific enthalpy, m^2/s^2
\tilde{k}	Specific kinetic turbulence energy, m^2/s^2
M	Mach number
M_{ij}	Component of specific tensor of fluctuating mass flux contribution, m^2/s^3
n_i	Component of wall-normal vector
p	Pressure, Pa
P_{ij}	Component of specific production tensor, m^2/s^3
q_i	Heat flux component, W/m^2
$q_i^{(t)}$	Turbulent heat flux component, W/m^2
\tilde{R}	Specific gas constant, $m^2/(s^2 K)$
\tilde{R}_{ij}	Specific Reynolds stress component, m^2/s^2
Re	Reynolds number
Re_t	turbulence Reynolds number
S_{ij}	Component of simple strain rate tensor, $1/s$
S_{ij}^*	Component of traceless strain rate tensor, $1/s$
S_l	length scale limiter in JHh-v2 model, m^2/s^4
$S_{\varepsilon 4}$	pressure gradient term in JHh-v2 model, m^2/s^4
T	Temperature, K
T_{ij}	Component of specific turbulent transport tensor, m^2/s^3
t	Time, s
U_i	Velocity component, m/s
u_i''	Fluctuating velocity component, m/s
u^+	Non-dimensional velocity in inner scaling
u_τ	Friction velocity, m/s
W_{ij}	Component of rotation tensor, $1/s$
x_i	Cartesian coordinates, m
y^+	Non-dimensional wall-distance in inner scaling
α	Incidence, <i>deg.</i>
α_ω	Coefficient of ω -production
β_ω	Coefficient of ω -destruction
γ	Ratio of specific heats
δ_0	Boundary layer thickness, m
δ_{ij}	Kronecker symbol
ε	Dissipation rate, m^2/s^3
ε^h	Homogeneous part of dissipation rate, m^2/s^3
ε_{ij}	Component of dissipation rate tensor, m^2/s^3
ζ	Argument to F_1 blending function
η	Non-dimensional spanwise coordinate
κ	Von Karman constant
λ	Heat conductivity, $kg m/(s^3 K)$
μ	Dynamic viscosity, $kg/(m s)$
ν	Kinematic viscosity, m^2/s
ρ	Density kg/m^3

σ_d	Coefficient of cross-diffusion
σ_ω	Coefficient of ω -diffusion
Π_{ij}	Component of specific pressure-strain correlation tensor, m^2/s^3
τ_{ij}	Viscous stress component, N/m^2
$\phi^{(\epsilon)}$	Coefficient belonging to ϵ -equation
$\phi^{(\omega)}$	Coefficient belonging to ω -equation
ω	Specific dissipation rate, $1/s$

I. Introduction

The development of new aircraft is expensive and often risky. In order to reduce the risk and time-to-market of future products, numerical simulation is regarded a key discipline. In particular Computational Fluid Dynamics (CFD) is considered essential for an optimum aerodynamic design of new aircraft within a reduced time frame.

However, relying more on simulation data increases the demand on the reliability of the underlying simulation results. The numerical accuracy can, at least in principle, be assured by refining the computational grid. Therefore, the accuracy of the employed physical models, especially the turbulence model, becomes of major importance. In particular, when approaching the borders of the flight envelope, increasingly complex flow phenomena, mainly associated with separation, are encountered, being a considerable challenge to the turbulence modeling.

Turbulence is characterized by a continuous spectrum of random fluctuations of all flow quantities in space and time. In principle, a prediction should be perfect when resolving the turbulent motion, whereby avoiding any modeling with its associated errors. Unfortunately, the smallest scales of turbulence become smaller with increasing Reynolds number, so that they are generally extremely small compared to the relevant geometrical scales of the aircraft. For this reason such Direct Numerical Simulations (DNS) will be unaffordable for realistic aeronautical flow problems for a long time.

The computational demand can be relaxed when resolving only the largest scales of turbulence by so-called Large Eddy Simulations (LES). In this case only the smallest scales have to be modeled for which simplifying assumptions hold, helping to keep the modeling error small. Nevertheless, as with DNS, the largest scale in an attached boundary layer is defined by the boundary-layer thickness which becomes very small at realistic flight Reynolds numbers. The need to resolve at least a certain range of turbulent scales with LES currently restricts its applicability to cases with massive separation at rather small Reynolds numbers.

In contrast, the classical way of tackling turbulent flows considers only the average or mean flow, where the average influence of turbulence has to be modeled, mainly in terms of additional, so-called Reynolds stresses and an additional turbulent heat flux. Based on the experience that the turbulent motion increases the lateral transport of heat and momentum, the most intuitive modeling approach is to increase the viscosity and the heat conductivity of the fluid by adding a so-called eddy viscosity and a so-called eddy heat conductivity which are no longer associated with the fluid but with the flow. With this so-called Boussinesq hypothesis the modeling task reduces to appropriately determine these parameters.

State-of-the-art models employ one or more transport equations for variables from which the eddy viscosity can be computed. From this the eddy heat conductivity is derived via the definition of a turbulent Prandtl number. Popular eddy viscosity models for aeronautical applications are the Spalart-Allmaras (SA) model,¹ relying on a modeled transport equation for the modified eddy viscosity, and the SST model by Menter,² relying on two transport equations for the kinetic turbulence energy and the so-called specific dissipation rate, respectively. In particular, the SST model has been sensitized to predict separation by an additional eddy viscosity limiter.

Eddy-viscosity-type RANS turbulence models can be efficiently solved by numerical methods and have proven to yield reliable results for attached boundary layer flows. Therefore they are the backbone of today's CFD simulations. Nevertheless the eddy viscosity approach is a drastic simplification of turbulence leading to a loss of accuracy in more complex flow situations.

Indeed the Boussinesq hypothesis assumes the Reynolds stresses being parallel to the viscous stresses, i.e. to the strain rate tensor, which is generally not the case. As long as there is only one dominating Reynolds stress component, as in simple boundary layers, the eddy viscosity can be appropriately calibrated. However in complex situations involving multiple interacting flow phenomena this approach is not adequate any

longer.

Thus, for meeting the requirements of simulation based aircraft design, improvements of the turbulence model's accuracy are needed that are still affordable in an industrial context. One development direction consists in so-called hybrid RANS/LES methods which aim at suitably combining some RANS model usually in attached boundary layers with some turbulence resolving method in separated regions where RANS models are known to fail. Prominent members of this class are the Detached Eddy Simulation (DES)³ and its derivatives, furthermore the Scale Adaptive Simulation (SAS)⁴ and the Partially Averaged Navier-Stokes approach (PANS).⁵ These techniques have shown to improve the simulation accuracy in case of massive separation at realistic Reynolds numbers. Nevertheless they remain expensive because of their need to resolve the unsteady turbulent motion reasonably well down to some small scale.

Therefore, in the current paper a different, purely RANS based approach is followed. Instead of approximating the Reynolds stresses by the Boussinesq hypothesis, the differential transport equation of the Reynolds stresses itself is employed, where the unknown terms are modeled. This allows for more accurate predictions of complex flows, because the Reynolds stresses can adapt more adequately in case of multiple interacting flow phenomena. Due to the higher number of equations involved, the computational cost of the so-called Reynolds stress models (RSM) is increasing, but only by a factor of roughly two per iteration, compared to the SST model.

II. Reynolds Stress Turbulence Modeling

II.A. Reynolds-Averaged Navier-Stokes Equations

For compressible flow it is most convenient to distinguish between simple averages, $\bar{\phi}$ indicated by an overbar, and mass weighted averages, $\tilde{\phi} = \overline{\rho\phi}/\bar{\rho}$, indicated by a tilde. The respective fluctuations are denoted by ϕ' and ϕ'' , where the single prime refers to simple and the double prime to mass weighted averaging.

With this notation the Reynolds-averaged Navier-Stokes equations read⁶

$$\frac{\partial \bar{\rho}}{\partial t} + \frac{\partial}{\partial x_k} (\bar{\rho} \tilde{U}_k) = 0, \quad (1)$$

$$\frac{\partial (\bar{\rho} \tilde{U}_i)}{\partial t} + \frac{\partial}{\partial x_k} (\bar{\rho} \tilde{U}_i \tilde{U}_k) + \frac{\partial}{\partial x_k} (\bar{\rho} \tilde{R}_{ik}) = -\frac{\partial \bar{p}}{\partial x_i} + \frac{\partial \bar{\tau}_{ik}}{\partial x_k}, \quad (2)$$

$$\frac{\partial (\bar{\rho} \tilde{E})}{\partial t} + \frac{\partial}{\partial x_k} (\bar{\rho} \tilde{H} \tilde{U}_k) + \frac{\partial}{\partial x_k} (\bar{\rho} \tilde{R}_{ik} \tilde{U}_i) = \frac{\partial (\bar{\tau}_{ik} \tilde{U}_i)}{\partial x_k} + \bar{\rho} D^{(k)} - \frac{\partial \bar{q}_k}{\partial x_x} - \frac{\partial \bar{q}_k^{(t)}}{\partial x_x} \quad (3)$$

with the averaged viscous stresses of a Newtonian fluid

$$\bar{\tau}_{ij} = 2\bar{\mu} \tilde{S}_{ij}^* = \bar{\mu} \left(\frac{\partial \tilde{U}_i}{\partial x_j} + \frac{\partial \tilde{U}_j}{\partial x_i} - \frac{2}{3} \frac{\partial \tilde{U}_k}{\partial x_k} \delta_{ij} \right) \quad (4)$$

and the Fourier type heat flux

$$\bar{q}_i = -\bar{\lambda} \frac{\partial \tilde{T}}{\partial x_i}. \quad (5)$$

The averaged molecular viscosity is provided by the Sutherland law

$$\frac{\bar{\mu}}{\mu_S} = \left(\frac{\tilde{T}}{T_S} \right)^{3/2} \frac{T_S + S}{\tilde{T} + S}, \quad (6)$$

where μ_S and T_S refer to a reference state and S is the Sutherland constant, taken to be $S = 110.4K$ for air.

An ideal gas is assumed, yielding

$$\bar{p} = \bar{\rho} R \tilde{T}, \quad (7)$$

where the specific gas constant for air is $R = 287 \text{m}^2/(\text{s}^2 \text{K})$. For an ideal gas the averaged specific total energy and total enthalpy are given by

$$\tilde{E} = \tilde{e} + \frac{1}{2} \tilde{U}_i \tilde{U}_i + \tilde{k}, \quad (8)$$

$$\tilde{H} = \tilde{E} + \frac{\tilde{p}}{\bar{\rho}} = \tilde{h} + \frac{1}{2} \tilde{U}_i \tilde{U}_i + \tilde{k}. \quad (9)$$

Assuming a perfect gas, the specific heats are constant, so that the averaged specific internal energy and enthalpy are given by

$$\tilde{e} = C_v \tilde{T}, \quad (10)$$

$$\tilde{h} = C_p \tilde{T}, \quad (11)$$

where for air $\gamma = C_p/C_v = 1.4$.

The underlined terms in the set of RANS equations (1) to (3) describe the average effect of turbulence on the mean flow and have to be modeled. The components of the Reynolds stress tensor

$$\overline{\rho \tilde{R}_{ij}} = \overline{\rho u_i'' u_j''} \quad (12)$$

represent the correlation of velocity fluctuations which are in the focus of any RANS modeling approach. Their thermal counterpart are the components of the turbulent heat flux vector

$$q_i^{(t)} = \overline{\rho h'' u_i''} \quad (13)$$

that represents a correlation between velocity and temperature fluctuations. Finally the term

$$\overline{\rho D^{(k)}} = \frac{\partial}{\partial x_k} \left(-\frac{1}{2} \overline{\rho u_i'' u_i'' u_k''} + \overline{\tau_{ik} u_i''} \right) \quad (14)$$

represents the diffusion of specific kinetic turbulence energy that is related to the Reynolds stresses by

$$\tilde{k} = \frac{1}{2} \tilde{R}_{ii}. \quad (15)$$

II.B. Reynolds Stress Transport Equation

From the exact momentum equation a transport equation for the Reynolds stresses can be derived, reading in general form⁶

$$\frac{\partial (\overline{\rho \tilde{R}_{ij}})}{\partial t} + \frac{\partial}{\partial x_k} (\overline{\rho \tilde{R}_{ij} \tilde{U}_k}) = \overline{\rho P_{ij}} + \overline{\rho \Pi_{ij}} - \overline{\rho \varepsilon_{ij}} + \overline{\rho D_{ij}} + \overline{\rho M_{ij}}, \quad (16)$$

where the production term

$$\overline{\rho P_{ij}} = -\overline{\rho \tilde{R}_{ik} \frac{\partial \tilde{U}_j}{\partial x_k}} - \overline{\rho \tilde{R}_{jk} \frac{\partial \tilde{U}_i}{\partial x_k}} \quad (17)$$

is exact since the mean flow velocity and the Reynolds stresses are provided by the equation system. In contrast, all other terms on the right hand side of Eq. (16) require modeling.

The most important term to be treated is the pressure-strain correlation

$$\overline{\rho \Pi_{ij}} = \overline{p' \left(\frac{\partial u_i''}{\partial x_j} + \frac{\partial u_j''}{\partial x_i} \right)} \quad (18)$$

which in case of an incompressible fluid represents a re-distribution of kinetic turbulence energy to the different directions. In compressible flow an additional pressure dilatation is included which, nevertheless, will be neglected here.

The dissipation term

$$\overline{\rho \varepsilon_{ij}} = \overline{\tau'_{ik} \frac{\partial u_j''}{\partial x_k}} + \overline{\tau'_{jk} \frac{\partial u_i''}{\partial x_k}} \quad (19)$$

represents the dissipation of turbulent fluctuations under the action of molecular viscosity.

The diffusion term

$$\overline{\rho D_{ij}} = \underbrace{-\frac{\partial}{\partial x_k} \left[\overline{\rho u_i'' u_j'' u_k''} \right]}_{\overline{\rho T_{ij}}} + \underbrace{\frac{\partial}{\partial x_k} \left[\left(\overline{\tau'_{ik} u_j''} + \overline{\tau'_{jk} u_i''} \right) \right]}_{\overline{\rho D_{ij}^{(\nu)}}} - \underbrace{\frac{\partial}{\partial x_k} \left[\left(\overline{p' u_i'' \delta_{jk}} + \overline{p' u_j'' \delta_{ik}} \right) \right]}_{\overline{\rho D_{ij}^{(p)}}} \quad (20)$$

contains contributions of turbulent transport, $\bar{\rho}T_{ij}$, viscous diffusion $\bar{\rho}D_{ij}^{(\nu)}$ and pressure diffusion $\bar{\rho}D_{ij}^{(p)}$, where the latter is considered negligible.⁶

Finally the term

$$\bar{\rho}M_{ij} = \bar{u}_i'' \left(-\frac{\partial \bar{p}}{\partial x_j} + \frac{\partial \bar{\tau}_{jk}}{\partial x_k} \right) + \bar{u}_j'' \left(-\frac{\partial \bar{p}}{\partial x_i} + \frac{\partial \bar{\tau}_{ik}}{\partial x_k} \right) \quad (21)$$

represents effects of compressibility that are negligible in transonic flows considered here. With this simplification the diffusion of kinetic turbulence energy, entering the total energy Eq. (3), is given by

$$\bar{\rho}D^{(\tilde{k})} = \frac{1}{2} \left(\bar{\rho}T_{ii} + \bar{\rho}D_{ii}^{(\nu)} \right). \quad (22)$$

Neglecting pressure dilatation, pressure diffusion, and contributions of the fluctuating mass flux, there remains the need for modeling the pressure-strain correlation, dissipation, turbulent transport, and viscous diffusion.

II.C. SSG/LRR- ω Turbulence Model

The SSG/LRR- ω has been developed within the framework of the European Project FLOMANIA⁷ for application to aeronautical flow problems.

II.C.1. Pressure-strain Correlation

The starting point for the pressure-strain correlation model suggested here has been devised by Speziale, Sarkar and Gatski (SSG)⁸ and reads

$$\begin{aligned} \bar{\rho}\Pi_{ij} = & - \left(C_1 \bar{\rho}\varepsilon + \frac{1}{2} C_1^* \bar{\rho}P_{kk} \right) \tilde{a}_{ij} + C_2 \bar{\rho}\varepsilon \left(\tilde{a}_{ik} \tilde{a}_{kj} - \frac{1}{3} \tilde{a}_{kl} \tilde{a}_{kl} \delta_{ij} \right) + \left(C_3 - C_3^* \sqrt{\tilde{a}_{kl} \tilde{a}_{kl}} \right) \bar{\rho} \tilde{k} \tilde{S}_{ij}^* \\ & + C_4 \bar{\rho} \tilde{k} \left(\tilde{a}_{ik} \tilde{S}_{jk} + \tilde{a}_{jk} \tilde{S}_{ik} - \frac{2}{3} \tilde{a}_{kl} \tilde{S}_{kl} \delta_{ij} \right) + C_5 \bar{\rho} \tilde{k} \left(\tilde{a}_{ik} \tilde{W}_{jk} + \tilde{a}_{jk} \tilde{W}_{ik} \right). \end{aligned} \quad (23)$$

For reasons of a consistent notation, the anisotropy tensor

$$\tilde{a}_{ij} = \frac{\tilde{R}_{ij}}{\tilde{k}} - \frac{2}{3} \delta_{ij} \quad (24)$$

is used instead of the anisotropy tensor \tilde{b}_{ij} proposed by Speziale, Sarkar and Gatski. The factor of 0.5, which occurs when transforming \tilde{b}_{ij} to \tilde{a}_{ij} , is included within the model coefficients.

$$\tilde{S}_{ij} = \frac{1}{2} \left(\frac{\partial \tilde{U}_i}{\partial x_j} + \frac{\partial \tilde{U}_j}{\partial x_i} \right), \quad (25)$$

$$\tilde{S}_{ij}^* = \tilde{S}_{ij} - \frac{1}{3} \tilde{S}_{kk} \delta_{ij} \quad (26)$$

are the components of the averaged simple and the traceless strain rate tensor, respectively, and

$$\tilde{W}_{ij} = \frac{1}{2} \left(\frac{\partial \tilde{U}_i}{\partial x_j} - \frac{\partial \tilde{U}_j}{\partial x_i} \right) \quad (27)$$

are the components of the averaged rotation tensor. The isotropic dissipation rate ε is provided by an additional transport equation for some length scale supplying variable. The C_i and C_i^* are model coefficients that have to be calibrated.

II.C.2. Dissipation

The dissipation is modeled by an isotropic tensor with the components

$$\bar{\rho}\varepsilon_{ij} = \frac{2}{3} \bar{\rho}\varepsilon, \quad (28)$$

where, as already said, the isotropic dissipation rate ε is provided by an additional transport equation for some length scale supplying variable. The deviatoric contributions are assumed to be already covered by the model of the pressure-strain correlation.

II.C.3. Diffusion

For the turbulent transport a generalized gradient diffusion model⁹

$$\bar{\rho}T_{ij} = \frac{\partial}{\partial x_k} \left(D \frac{\bar{\rho}\tilde{k}\tilde{R}_{kl}}{\varepsilon} \frac{\partial \tilde{R}_{ij}}{\partial x_l} \right) \quad (29)$$

is invoked, where D is a diffusion coefficient. Since the components of the viscous diffusion tensor are given by

$$\bar{\rho}D_{ij}^{(\nu)} = \frac{\partial}{\partial x_k} \left(\frac{\partial \tilde{R}_{ij}}{\partial x_k} \right), \quad (30)$$

both contributions can be combined, yielding

$$\bar{\rho}D_{ij} = \frac{\partial}{\partial x_k} \left[\left(\bar{\mu}\delta_{ij} + D \frac{\bar{\rho}\tilde{k}\tilde{R}_{kl}}{\varepsilon} \right) \frac{\partial \tilde{R}_{ij}}{\partial x_l} \right] \quad (31)$$

for the components of the turbulent diffusion tensor.

II.C.4. Length Scale Equation

As with two-equation eddy viscosity models, an additional transport equation is required for closing the equation system for providing a measure of the isotropic dissipation rate ε . Most Reynolds stress models employ the isotropic dissipation rate ε , as there is a transport equation for this quantity that can be derived analytically.⁶ In contrast, the SSG/LRR- ω model follows Menter's approach,² combining the ε -equation at the outer edge of the boundary layer with Wilcox' ω -equation¹⁰ near the wall by blending the coefficients. This so-called BSL- ω -equation has been very successful in conjunction with Menter's SST model² and reads

$$\frac{\partial(\bar{\rho}\omega)}{\partial t} + \frac{\partial}{\partial x_k} (\bar{\rho}\omega\tilde{U}_k) = -\alpha_\omega \frac{\omega}{\tilde{k}} \frac{\bar{\rho}P_{kk}}{2} - \beta_\omega \bar{\rho}\omega^2 + \frac{\partial}{\partial x_k} \left[\left(\bar{\mu} + \sigma_\omega \frac{\bar{\rho}\tilde{k}}{\omega} \right) \frac{\partial \omega}{\partial x_k} \right] + \sigma_d \frac{\bar{\rho}}{\omega} \max \left(\frac{\partial \tilde{k}}{\partial x_k} \frac{\partial \omega}{\partial x_k}, 0 \right), \quad (32)$$

where the isotropic dissipation rate is provided by

$$\varepsilon = C_\mu \tilde{k}\omega \quad (33)$$

with $C_\mu = 0.09$.

The coefficients $\phi = \alpha_\omega, \beta_\omega, \sigma_\omega, \sigma_d$ are blended according to

$$\phi = F_1 \phi^{(\omega)} + (1 - F_1) \phi^{(\varepsilon)} \quad (34)$$

between the values associated with the ω - and ε -equation, respectively, where the blending function is given by

$$F_1 = \tanh(\zeta^4) \quad (35)$$

with the argument

$$\zeta = \min \left[\max \left(\frac{\sqrt{\tilde{k}}}{C_\mu \omega d}, \frac{500 \bar{\mu}}{\bar{\rho} \omega d^2} \right), \frac{4 \sigma_\omega^{(\varepsilon)} \bar{\rho} \tilde{k}}{\sigma_d^{(\varepsilon)} \frac{\bar{\rho}}{\omega} \max \left(\frac{\partial \tilde{k}}{\partial x_k} \frac{\partial \omega}{\partial x_k}, 0 \right) d^2} \right]. \quad (36)$$

The bounding values of the coefficients are provided in Table 1.

Table 1. Bounding Values of ω -Equation Coefficients for SSG/LRR- ω Model

	α_ω	β_ω	σ_ω	σ_d
$\phi^{(\varepsilon)}$	0.44	0.0828	0.856	1.712
$\phi^{(\omega)}$	0.5556	0.075	0.5	0

II.C.5. Near-wall extension of Reynolds stress model terms

As one can see, all modeled terms in the Reynolds stress equation involve the isotropic dissipation rate ε , making them dependent on the employed length scale equation. Since the SSG model has been developed based on an ε -equation, some near-wall modification is required, when coupling it with the BSL ω -equation, approaching the ω -equation at the wall.

As Wilcox⁶ has shown, the Launder-Reece-Rodi (LRR) model¹¹ can be easily combined with an ω -equation, when omitting the wall-reflexion terms. The corresponding pressure-strain correlation can be transformed into the same form as Eq. (23) so that the same blending technique can be applied as to the coefficients of the BSL ω -equation. The same holds for the diffusion coefficient D . Due to this near-wall modification the model is termed SSG/LRR- ω model.¹²

The bounding values, indicated by SSG and LRR, are given in Table 2. Note that the values of D and $c_2^{(LRR)}$ have been slightly modified with respect to Ref.¹², in order to achieve better agreement with the log layer of a zero pressure gradient boundary layer.

Table 2. Bounding Values of the SSG/LRR- ω Model Term Coefficients ($c_2^{(LRR)} = 0.52$)

	C_1	C_1^*	C_2	C_3	C_3^*	C_4	C_5	D
SSG	1.7	0.9	1.05	0.8	0.65	0.625	0.2	0.22
LRR	1.8	0	0	0.8	0	$\frac{9c_2^{(LRR)}+6}{11}$	$\frac{-7c_2^{(LRR)}+10}{11}$	$0.75C_\mu$

II.D. JHh-v2 Turbulence Model

The JHh-v2 Reynolds-stress model is a modified version of the JHh model developed by Jakirlić and Hanjalić,¹³ which uses the homogeneous dissipation rate ε^h as length scale variable in order to capture the correct dissipation rate profile close to walls. Probst¹⁴ extended the length scale equation by two additional source terms, gaining promising results in different subsonic aerodynamic flows. For the application of the model to subsonic as well as transonic aerodynamic flows, an adaptation of coefficients in the length scale equation was conducted, furthermore a quadratic extension of the slow redistribution term¹⁵ was added.

II.D.1. Pressure-strain Correlation

The JHh-v2 RSM employs a linear pressure-strain correlation which is extended by a quadratic formulation of the slow redistribution term as well as by a wall-reflection model Π_{ij}^w according to Gibson and Launder:¹⁶

$$\bar{\rho}\Pi_{ij} = \bar{\rho}\Pi_{ij,1} + \bar{\rho}\Pi_{ij,1}^w + \bar{\rho}\Pi_{ij,2} + \bar{\rho}\Pi_{ij,2}^w \quad (37)$$

$$\bar{\rho}\Pi_{ij,1} = -\varepsilon^h \bar{\rho} \left[\hat{C}_1 \tilde{a}_{ij} + \hat{C}'_1 \left(\tilde{a}_{ik} \tilde{a}_{jk} - \frac{1}{3} \delta_{ij} A_2 \right) \right] \quad (38)$$

$$\bar{\rho}\Pi_{ij,2} = -\hat{C}_2 \bar{\rho} \left(P_{ij} - \frac{1}{3} P_{kk} \delta_{ij} \right) \quad (39)$$

$$\bar{\rho}\Pi_{ij,1}^w = \hat{C}_1^w \bar{\rho} f_w \frac{\varepsilon^h}{k} \left(\tilde{R}_{km} n_k n_m \delta_{ij} - \frac{3}{2} \tilde{R}_{ik} n_k n_j - \frac{3}{2} \tilde{R}_{kj} n_k n_i \right) \quad (40)$$

$$\bar{\rho}\Pi_{ij,2}^w = \hat{C}_2^w \bar{\rho} f_w \left(\Pi_{km,2} n_k n_m \delta_{ij} - \frac{3}{2} \Pi_{ik,2} n_k n_j - \frac{3}{2} \Pi_{kj,2} n_k n_i \right) \quad (41)$$

For the wall-reflection model, wall normals n_i must be provided within the flowfield. The model coefficients contain near-wall damping functions which are calibrated based on DNS data:

$$\hat{C}_1 = \hat{C} + \sqrt{AE^2}, \quad \hat{C}'_1 = -\max(0.7A_2; 0.5) \hat{C}_1, \quad \hat{C}_2 = 0.8A^{1/2}, \quad \hat{C} = 2.5AF^{1/4} f, \quad F = \min(0.6; A_2),$$

$$f = \min \left[(\text{Re}_t / 150)^{3/2}; 1 \right], \quad \hat{C}_1^w = \max \left(1 - 0.7\hat{C}; 0.3 \right), \quad \hat{C}_2^w = \max(A; 0.3), \quad f_w = \min \left[\frac{\tilde{k}^{3/2}}{2.5\varepsilon^h d}; 1.4 \right]. \quad (42)$$

These damping functions comprise the turbulence Reynolds number $\text{Re}_t = \tilde{k}^2 / (\nu \varepsilon^h)$, the turbulent kinetic energy \tilde{k} , the local wall distance d as well as anisotropy invariants of the Reynolds stress tensor and the

homogeneous dissipation rate tensor:

$$A = 1 - \frac{9}{8}(A_2 - A_3) \quad \text{with} \quad A_2 = \tilde{a}_{ij}\tilde{a}_{ji}, \quad A_3 = \tilde{a}_{ij}\tilde{a}_{jk}\tilde{a}_{ki}, \quad \tilde{a}_{ij} = \frac{\tilde{R}_{ij}}{\tilde{k}} - \frac{2}{3}\delta_{ij} \quad (43)$$

$$E = 1 - \frac{9}{8}(E_2 - E_3) \quad \text{with} \quad E_2 = e_{ij}e_{ji}, \quad E_3 = e_{ij}e_{jk}e_{ki}, \quad e_{ij} = \frac{\varepsilon_{ij}^h}{\varepsilon^h} - \frac{2}{3}\delta_{ij} \quad (44)$$

II.D.2. Dissipation

The anisotropic dissipation rate tensor ε_{ij} can be divided into a homogeneous part and a non-homogeneous part

$$\varepsilon_{ij} = \varepsilon_{ij}^h + \frac{1}{2}D_{ij}^\nu, \quad (45)$$

wherein the homogeneous part is approximated by an implicit relation:

$$\varepsilon_{ij}^h = f_s \tilde{R}_{ij} \frac{\varepsilon^h}{\tilde{k}} + (1 - f_s) \frac{2}{3} \delta_{ij} \varepsilon^h \quad \text{with} \quad f_s = 1 - \sqrt{AE^2}. \quad (46)$$

The homogeneous dissipation rate ε^h is provided by a scalar length scale equation.

II.D.3. Diffusion

The turbulent diffusion is modelled by the same tensor (31) used for the SSG/LRR- ω model, the coefficient D equals the SSG bounding value of 0.22.

II.D.4. Length Scale Equation

As length-scale variable, the homogeneous part ε^h of the dissipation rate is chosen:

$$\frac{D\varepsilon^h}{Dt} = -\hat{C}_{\varepsilon 1} \frac{\varepsilon^h}{\tilde{k}} \tilde{R}_{ij} \frac{\partial \tilde{U}_i}{\partial x_j} - \hat{C}_{\varepsilon 2} f_\varepsilon \frac{\varepsilon^h \tilde{\varepsilon}^h}{\tilde{k}} + \hat{C}_{\varepsilon 3} \nu \frac{\tilde{k}}{\varepsilon^h} \tilde{R}_{jk} \frac{\partial^2 \tilde{U}_i}{\partial x_j \partial x_l} \frac{\partial^2 \tilde{U}_i}{\partial x_k \partial x_l} + \frac{\partial}{\partial x_k} \left[\left(\frac{1}{2} \nu \delta_{kl} + \hat{C}_\varepsilon \frac{\tilde{k}}{\varepsilon^h} \tilde{R}_{kl} \right) \frac{\partial \varepsilon^h}{\partial x_l} \right] + S_l + S_{\varepsilon 4} \quad (47)$$

with the low-Reynolds damping function

$$f_\varepsilon = 1 - \frac{C_{\varepsilon 2} - 1.4}{C_{\varepsilon 2}} \exp \left[- \left(\frac{R\epsilon_t}{6} \right)^2 \right]. \quad (48)$$

Two additional source terms have been introduced into the length-scale equation, namely the length-scale limiter

$$S_l = \max \left\{ \left[\left(\frac{1}{C_l} \frac{\partial l}{\partial x_n} \right)^2 - 1 \right] \left(\frac{1}{C_l} \frac{\partial l}{\partial x_n} \right)^2 ; 0 \right\} \frac{\varepsilon^h \tilde{\varepsilon}^h}{\tilde{k}} A \quad \text{with} \quad C_l = 2.5 \quad , \quad l = \frac{\tilde{k}^{3/2}}{\varepsilon} \quad (49)$$

and the pressure-gradient term

$$S_{\varepsilon 4} = -\hat{C}_{\varepsilon 4}^* \frac{\varepsilon^h}{\tilde{k}} \left(\tilde{R}_{ss} \frac{\partial \tilde{U}_s}{\partial x_s} + \tilde{R}_{n_1 n_1} \frac{\partial \tilde{U}_{n_1}}{\partial x_{n_1}} + \tilde{R}_{n_2 n_2} \frac{\partial \tilde{U}_{n_2}}{\partial x_{n_2}} \right), \quad (50)$$

to sensitize the equation to effects of non-equilibrium turbulence.¹⁴ The source term $S_{\varepsilon 4}$ needs to be computed in streamline oriented coordinates (x_s, x_{n_1}, x_{n_2}) . The coefficients used in the length scale equation are provided in table 3.

Table 3. Coefficients of the ε^h -Equation for the JHh-v2 Model

$\hat{C}_{\varepsilon 1}$	$\hat{C}_{\varepsilon 2}$	$\hat{C}_{\varepsilon 3}$	$\hat{C}_{\varepsilon 4}^*$	\hat{C}_{ε}
1.44	1.85	0.70	0.58	0.18

III. Results

The above mentioned models have been implemented into DLR's TAU code,¹⁷ solving the RANS equations on hybrid unstructured grids with second order accuracy. Standard numerics include a central discretization of the convective RANS terms with artificial dissipation, whereas first or second order upwinding is used for the turbulence equations. Alternatively, low dissipation second order upwind schemes like AUSMDV can be used for the whole set of equations. Integration is carried out either by an explicit three-stage Runge-Kutta or an implicit LUSGS scheme, both accelerated by multigrid. As it appears, the Reynolds stress models show some sensitivity to grid imperfections. Nevertheless, after modifying regions that have been identified as critical, there seems to be no general problem to solving the complete set of equations for aeronautical applications.

III.A. Zero Pressure Gradient Flat Plate

A standard test case any turbulence model for aeronautical applications has to withstand is the flow over a zero pressure gradient flat plate. In particular the velocity profile is checked for agreement with the so-called log-law⁶

$$u^+ = \frac{1}{\kappa} \ln y^+ + C, \quad (51)$$

with the non-dimensional velocity and wall-distance

$$u^+ = \frac{\tilde{U}}{u_\tau} \quad (52)$$

$$y^+ = \frac{y u_\tau}{(\bar{\mu}/\bar{\rho})_w} \quad (53)$$

and the friction velocity

$$u_\tau = \sqrt{\left(\frac{\bar{\tau}}{\bar{\rho}}\right)_w}. \quad (54)$$

The von Kármán constant is usually taken to be $\kappa = 0.41$, and the coefficient $C = 5 \dots 5.5$. In the viscous sublayer, i.e. for $y^+ \leq 3 \dots 5$ the velocity profile must follow the relation

$$u^+ = y^+. \quad (55)$$

Fig. 1 (left) shows the log-linear plot of the velocity profile on a zero pressure gradient flat plate predicted by the Reynolds stress models compared to the above log-law (52) with $C = 5.25$ and the viscous sublayer solution (55). Additionally the results for the Spalart-Allmaras model in its original version (SAO) and the SST model are plotted for comparison. As one can see, the velocity profiles predicted by the SSG/LRR- ω model and the SST model are almost identical, showing a slightly steeper log-law than theoretically expected. However the SAO model and the JHh-v2 model yield velocity profiles that adapt more rapidly to the log-law, probably due to their particular calibration of the wall-damping.

Fig. 1 (right) shows the corresponding skin friction distributions compared to the experiments by Wieghardt.¹⁸ The Reynolds stress models and the SST model yield virtually identical results, whereas the SAO model gives slightly higher skin friction.

These results prove the applicability of the SSG/LRR- ω RSM, i.e. the LRR extension of the SSG model employing the BSL ω -equation, to the near-wall region of wall-bounded flows without using wall-functions or near-wall damping. On the other hand, the suitability of the near-wall damping functions in the JHh-v2 RSM are demonstrated as well.

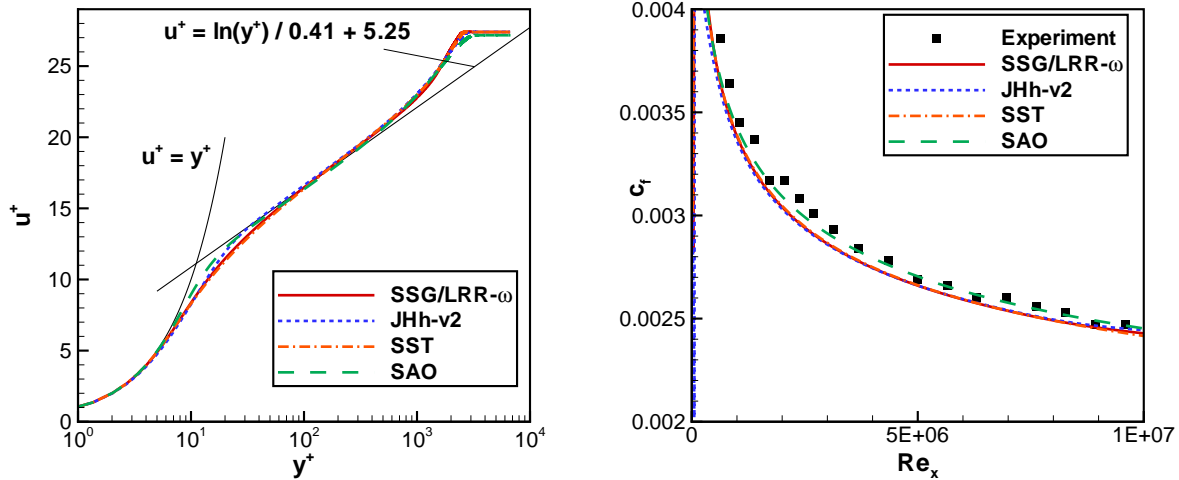


Figure 1. Zero pressure gradient flat plate. Velocity profile (left) and skin friction (right).

III.B. Oblique Shock/Boundary-Layer Interaction

In order to investigate the performance of the turbulence models in shock-induced separation, the interaction of an oblique shock with a flat plate boundary layer is simulated. Numerous experiments have been carried out at the Institut Universitaire des Systèmes Thermiques Industriels (IUSTI), Marseille, France, using a supersonic wind tunnel at Mach 2.3.^{19,20} This test case has furthermore been numerically investigated with Large Eddy Simulation, e.g. by Garnier et al.²¹ as well as Touber and Sandham.²² The shock, created by a sharp-edged plate which is placed with an angle of 8 degrees into the freestream, is strong enough to force a separation of the turbulent boundary layer.

Numerical simulations have been conducted using the Reynolds stress models SSG/LRR- ω and JHh-v2 as well as the eddy viscosity models Menter SST and Spalart-Allmaras (SAO), on a structured mesh with 380x200 grid points. The simulated shock-wave/boundary-layer interaction region can be seen in Fig. 2. The

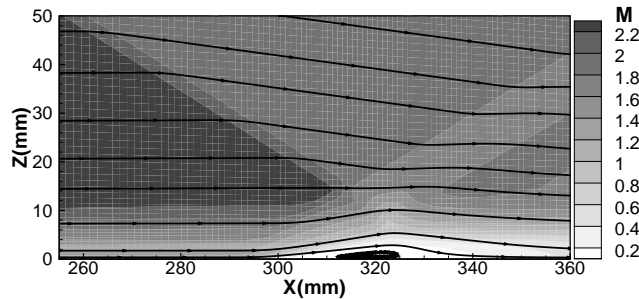


Figure 2. Oblique Shock Boundary Layer Interaction, $M = 2.3$. Flowfield simulated with the SSG/LRR- ω model.

size of the shock-induced separation shows a high sensitivity towards the incoming boundary layer thickness, which was adapted by varying the length of the computational domain upstream of the interaction region. The boundary layer thickness measured in the experiments upstream of the interaction region is indicated as $\delta_0 = 11$ mm, the skin friction equals $c_f = 0.002$. The corresponding properties of the inflow boundary layers in the numerical simulations are listed in table 4.

Figure 3 shows the simulated velocity profiles of the boundary layer at different streamwise positions, in comparison to PIV data by Dupont et al.²⁰ and LES data by Touber and Sandham.²² At the first position, which is located directly upstream the interaction region, the good agreement of the simulated and measured inflow boundary layers can be seen.

Table 4. Boundary layer thickness and skin friction upstream of the interaction region, $X = 260$ mm

	SSG/LRR- ω	JHh-v2	Menter SST	SAO
δ_0 (mm)	10.94	10.97	10.94	11.05
c_f	0.00203	0.00200	0.00202	0.00214

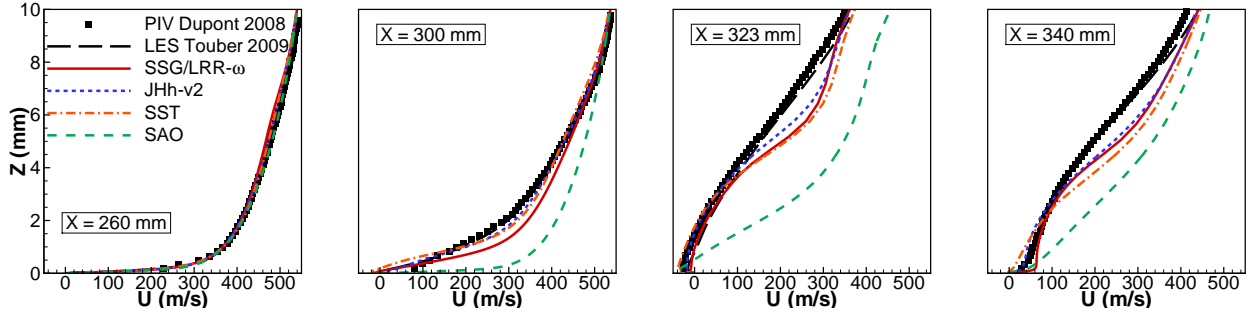


Figure 3. Oblique Shock Boundary Layer Interaction, $M = 2.3$. Velocity profiles at different streamwise positions.

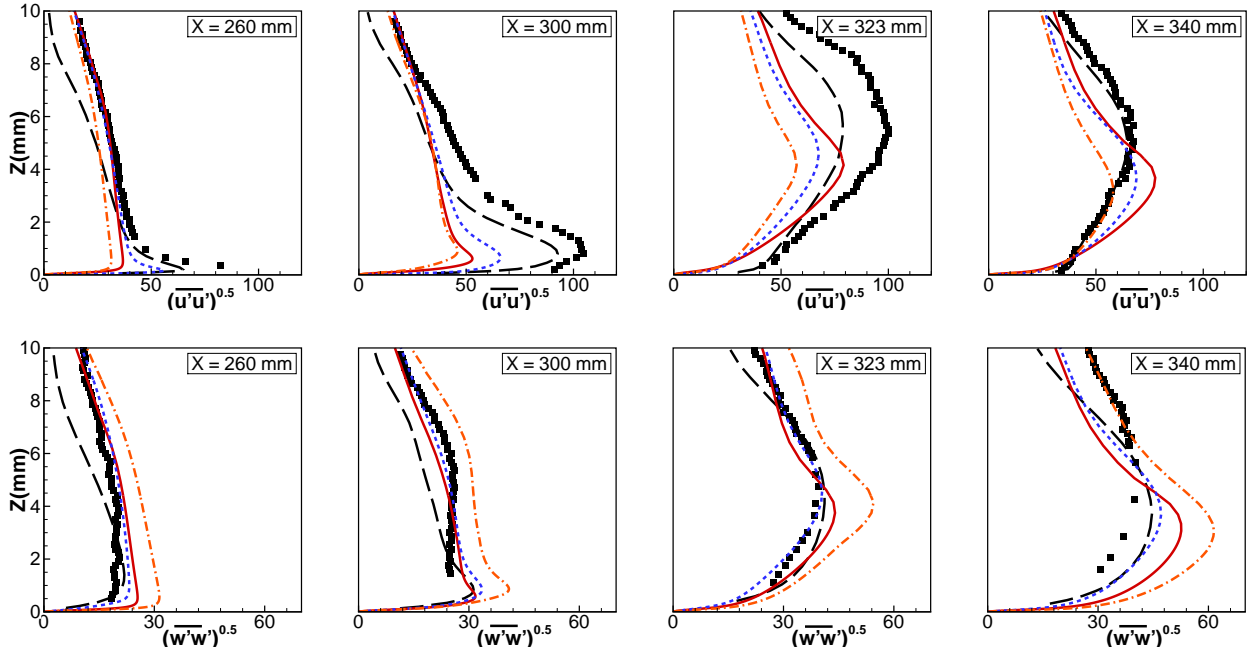


Figure 4. Oblique Shock Boundary Layer Interaction, $M = 2.3$. $\sqrt{\tilde{R}_{11}}$ and $\sqrt{\tilde{R}_{33}}$ profiles at different streamwise positions.

While the SAO model considerably fails to predict the momentum loss as well as the profile of the boundary layer, the other turbulence models show a quite similar global behavior. The dimension of the interaction region is underestimated by all turbulence models, hence the pressure rise starts further downstream. As a consequence, already at $X = 300$ mm the experimental boundary layer is stronger decelerated as the simulated ones. The velocity profile inside the separation is shown at the third boundary layer position ($X = 323$ mm). The near-wall region of the simulated boundary layers is still decelerated, while the outer part is already accelerated. This leads to a curved velocity profile with two inflection points, which is not observable in the rather smooth experimental velocity profile. These tendencies are more distinct in Menter SST solutions than in Reynolds stress solutions. Nonetheless the near-wall region including the shock-induced separation is well reproduced by the Reynolds stress models and by the SST model. The same boundary layer characteristics can be found further downstream at $X = 340$ mm, with the best estimation of the near-wall velocity by the JHh-v2 model.

Figure 4 gives wall normal distributions of the square root of the Reynolds stress components $(\tilde{R}_{11})^{0.5}$ and $(\tilde{R}_{33})^{0.5}$, respectively, simulated with the Reynolds stress models as well as the SST model in comparison to PIV and LES data. The Reynolds stress distributions of the SST results are calculated via the compressible Boussinesq hypothesis. Here the improved modeling of turbulent stresses within the differential Reynolds stress models, especially their capability of accounting for Reynolds stress anisotropy, is clearly visible. The SSG/LRR- ω model and the JHh-v2 model predict higher levels of turbulent stress in streamwise direction than in wall-normal direction, which is confirmed by the experiment. As a result of its inherent assumption of stress isotropy, the SST model is unable to capture these differences. Upstream of the shock ($X = 260$ mm), an improved estimation of the characteristic near-wall Reynolds stress peak in streamwise direction can be seen when simulating with the JHh-v2 RSM, due to its modeling of near-wall blockage of normal fluctuations.

Inside the interaction region, all turbulence models predict smaller streamwise Reynolds stress levels than the experiment. Furthermore the maximum of Reynolds stresses is found closer to the wall, caused by the increased velocity gradient in wall-normal direction. Towards the end of the interaction region, the Reynolds stress models show qualitatively reasonable maximum values of $(\tilde{R}_{11})^{0.5}$. The turbulent stress levels in wall-normal direction simulated with the Reynolds stress models are in a good agreement with the experimental data, showing only a slight overestimation towards the end of the interaction region. This tendency is more distinct with the SSG/LRR- ω model.

III.C. HGR-01 Airfoil at Stall

As a subsonic test case relevant to aeronautical applications, the 2D tail-plane research airfoil HGR-01 is considered for validating the differential stress models. Experimental data²³ at a Mach number of $M = 0.073$ and a Reynolds number of $Re = 0.6565 \cdot 10^6$ show a mixed stall behavior with both laminar leading-edge separations and turbulent separations from the trailing edge. However, up to beyond maximum lift at $\alpha = 12^\circ$ the flow is dominated by a gradually growing trailing-edge separation which therefore represents the focus of the investigation. The simulations employ the hybrid grid depicted in Fig. 5 with 650×112 points in the structured near-wall part, which extends into the wake (c-topology) to accurately resolve the trailing-edge flow region. Mesh refinement studies applying a systematic variation of the cell sizes suggest virtually grid-independent results for the 2nd-order spatial schemes used in the DLR TAU code.

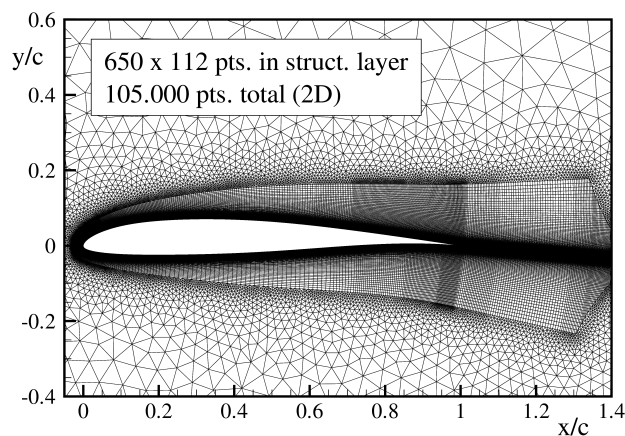


Figure 5. HGR-01 airfoil. 2D hybrid c-type mesh.

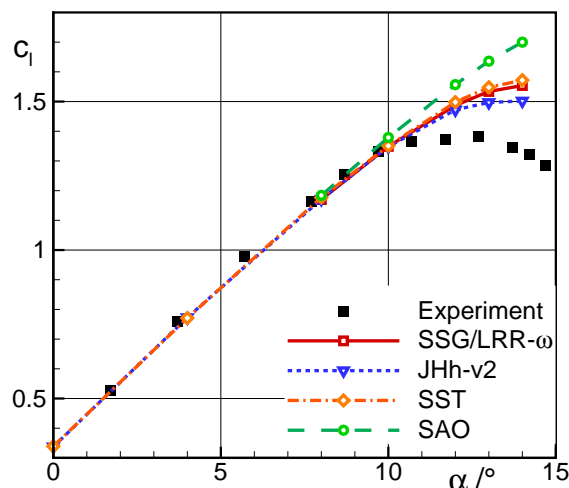


Figure 6. HGR-01 airfoil. Lift curve, $M = 0.073$, $Re = 656500$.

A comparison of numerically simulated lift-over- α curves with experimental data is shown in Fig. 6. While all four models overestimate the measured lift coefficient at high angles of attack, only the JHh-v2 RSM reaches a maximum value within the considered α -regime and predicts $c_{l,max}$ just by about $\Delta c_l \approx 0.1$ higher than measured. Similar to the k- ω SST model the SSG/LRR- ω RSM at least approaches a stagnation limit, whereas the Spalart-Allmaras one-equation model drastically overshoots stall onset.

Accordingly, the SAO model departs very strongly from the measured velocity and Reynolds-shear-stress profiles at $\alpha = 12^\circ$, which are compared with PIV data at two streamwise stations in Fig. 7 and 8. The

other models – most notably the JHh-v2 RSM – predict the momentum loss and thickness of the decelerated boundary-layer at $x/c = 0.7$ rather well. Moreover, the magnitude of turbulent shear stress is captured best by the two RSMs. At $x/c = 0.95$, however, the experimental data exhibit a pronounced separation region, whereas all simulations predict attached flow and underestimate the level of Reynolds shear stress. Regardless of the lacking backflow region near the wall, the boundary-layer thickness at this station is almost matched by the JHh-v2 model which explains its somewhat better agreement with the measured lift curve.

To summarize the findings, the differential stress approach offers slight to moderate improvements of low-speed airfoil-stall predictions compared to conventional eddy viscosity models, although it remains a challenging test. Note that the original calibration of the JHh-v2 RSM according to¹³ was shown to predict earlier separation onset and lift breakdown in closer agreement to the experiment.¹⁴ However, due to unsatisfying results for the transonic flow cases presented in this paper, that model variant was considered less suited for general aeronautical applications.

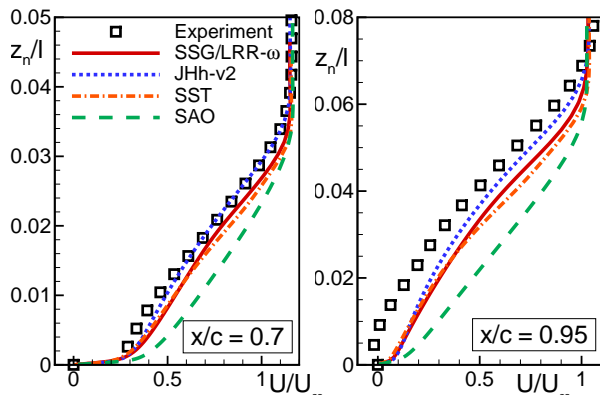


Figure 7. HGR-01 airfoil. Velocity profiles at $x/c = 0.70$ (left) and $x/c = 0.95$ (right), $\alpha = 12^\circ$, $M = 0.073$, $Re = 656500$.

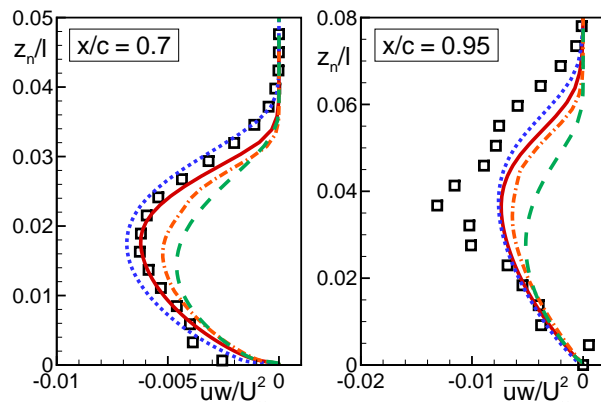


Figure 8. HGR-01 airfoil. Reynolds-shear-stress profiles at $x/c = 0.70$ (left) and $x/c = 0.95$ (right), $\alpha = 12^\circ$, $M = 0.073$, $Re = 656500$.

III.D. RAE 2822 Airfoil

The flow around the RAE 2822 airfoil is a standard test case for turbulence models in transonic flow.²⁴ In particular the so-called Case 9 with Mach number $M = 0.73$, Reynolds number $Re = 6.5 \cdot 10^6$ and the so-called Case 10 with Mach number $M = 0.75$ and Reynolds number $Re = 6.2 \cdot 10^6$ are interesting, where in both cases the incidence is $\alpha = 2.8^\circ$ and transition is prescribed at 3% chord on both sides. In the experiment the shock is located at virtually the same position under both flow conditions, whereas numerical simulations usually yield different shock positions, depending on the turbulence model.

Computations have been carried out with the DLR TAU code. For the turbulence models SSG/LRR- ω , Menter SST and SAO a structured mesh of 736×176 cells was used, the simulations with the JHh-v2 model ran on a hybrid grid with 700×176 cells in the structured near-wall part. Both meshes allow for fairly grid converged solutions. Fig. 9 shows the pressure distributions obtained with the different turbulence models compared to the experiment. As one can see, the SAO model predicts the shock position for Case 9 in good agreement with the experiment, whereas for Case 10 the shock is found considerably downstream the experimental position. In contrast, the SST model and both Reynolds stress models predict the shock for Case 9 slightly upstream and for Case 10 slightly downstream the experimental position, which appears as the superior result.

In addition, Fig. 10 shows the corresponding skin friction distributions. Ahead of the shock, the Reynolds stress models and the SST model yield virtually the same local skin friction coefficient, whereas the SAO model gives slightly higher $c_{f,loc}$ -values, indicating a thinner boundary layer. Behind the shock, the model predictions differ, but the experimental data are too sparse for any sensible assessment.

III.E. ONERA M6 Wing

The ONERA M6 wing can be considered the three-dimensional counterpart to the RAE 2822 airfoil, addressing the prediction of transonic flow, including shock-induced separation.²⁵ The case investigated here refers

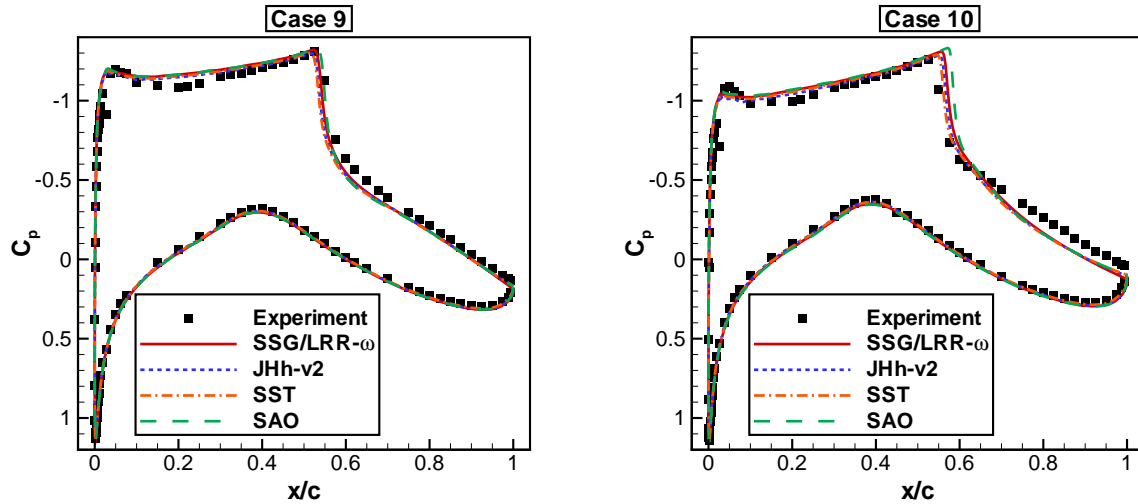


Figure 9. RAE 2822 airfoil. Pressure distributions for Case 9 (left) and Case 10 (right).

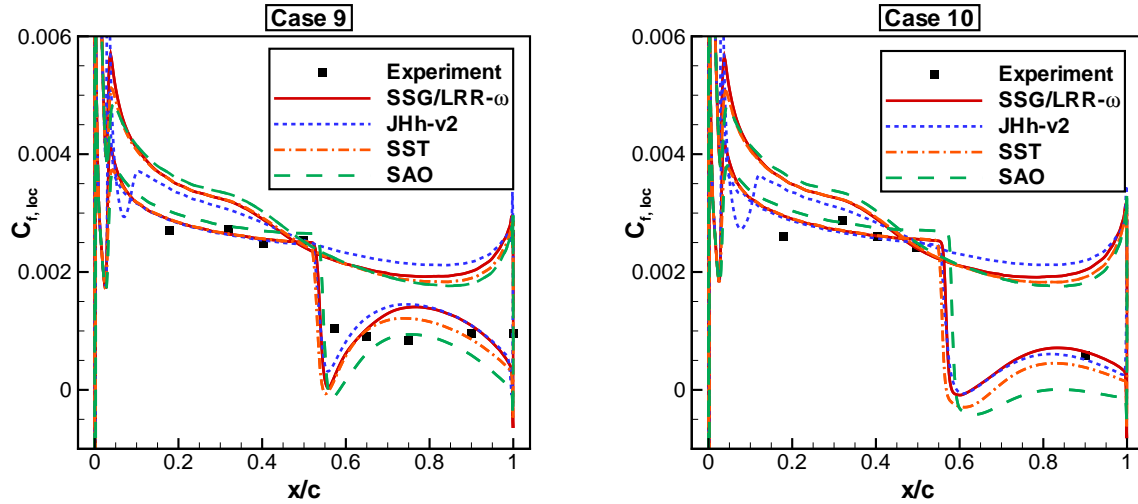


Figure 10. RAE 2822 airfoil. Skin friction distributions for Case 9 (left) and Case 10 (right).

to the experiments carried out at a Mach number of $M = 0.84$ and a Reynolds number of $Re = 11.72 \cdot 10^6$, where the incidence was varied in the range $0.03^\circ \leq \alpha \leq 6.06^\circ$. Computations have been carried out with the DLR TAU code, the resolution of the wing surfaces are shown in Fig. 11. For the turbulence models SSG/LRR- ω , Menter SST and SAO a hybrid grid with $4.6 \cdot 10^6$ nodes was used (Fig. 11 left), the simulation with the JHh-v2 model ran on a hexahedral grid with $1.8 \cdot 10^6$ nodes (Fig. 11 right).

Up to an incidence of $\alpha = 3.06^\circ$ there is hardly any difference between the predictions by different turbulence models. However at $\alpha = 4.08^\circ$ the results for Reynolds stress models deviate considerably from the eddy viscosity model results in the outboard part of the wing. Fig. 12 shows the predicted pressure distributions in two outboard sections at 80% and 95% span. As one can see, the Spalart-Allmaras (SAO) and SST model predictions deviate significantly from the experimental results, whereas the pressure distribution predicted by the SSG/LRR- ω model is in rather good agreement with the measurements in both sections. The shock position predicted by the JHh-v2 RSM is even in a better agreement with experimental results at 80% span, in contrast at 95% span the deviations grow significantly.

Fig. 13 explains the difference, showing the friction line pattern on the upper surface of the wing. As

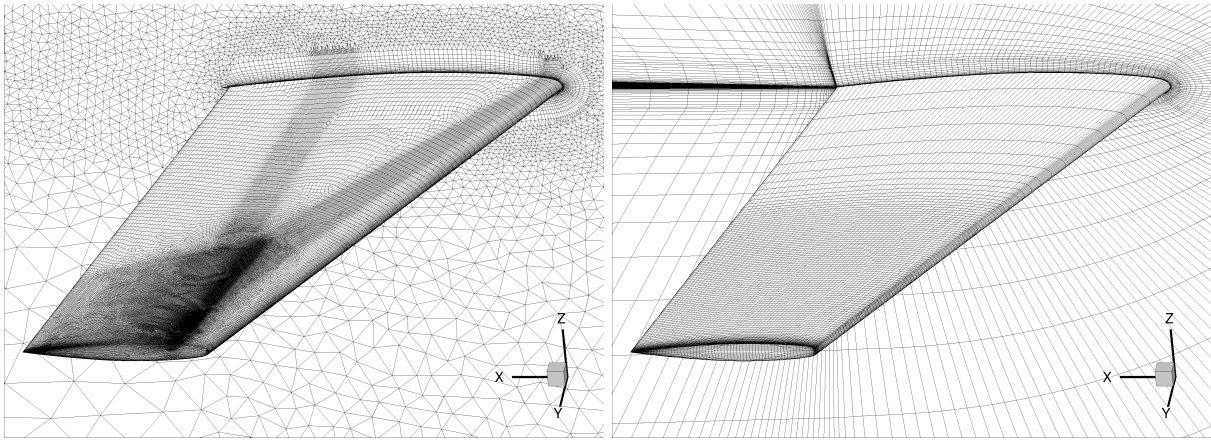


Figure 11. ONERA M6 wing. Grid resolution of the surfaces for computations with the models SSG/LRR- ω , SST and SAO (left) and JHh-v2 (right).

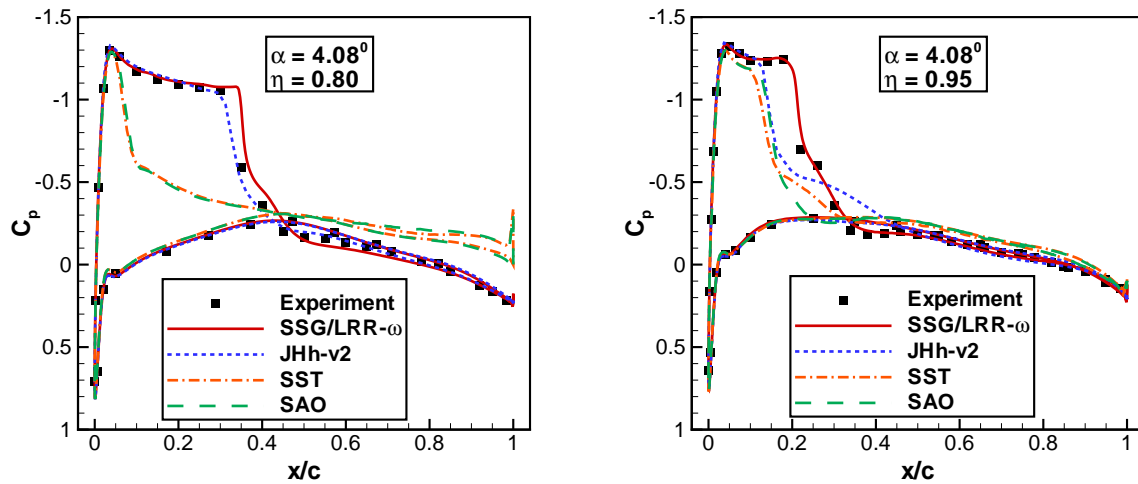


Figure 12. ONERA M6 wing. Pressure distribution at incidence $\alpha = 4.08^\circ$ in two outboard sections at $\eta = 0.80$ (left) and $\eta = 0.95$ (right).

one can see, with the SST model a largely separated flow is predicted on the outer half of the wing, whereas with the SSG/LRR- ω model the separation is limited to a small zone behind the shock foot. According to the pressure distribution, this behavior is in better agreement with the experiment.

The spanwise extension of separated flow becomes smaller using the JHh-v2 RSM, however the reattachment line is found downstream of the SSG/LRR- ω results.

IV. Conclusion

Two differential Reynolds stress models for aeronautical applications have been presented: The SSG/LRR- ω model blends the SSG pressure-strain correlation into the LRR pressure-strain near walls and employs Menter's BSL ω -equation. The JHh-v2 model is a modified version of the JHh model by Jakirlić and Hanjalić based on a length-scale equation for the homogeneous part of the dissipation rate ε^h .

Results presented for the flat plate show good agreement of the predicted velocity profile with the log-law. While the skin friction predicted with the both Reynolds stress models is in close co-incidence with the SST model, it is slightly lower than with the SAO model.

Regarding the shock-wave/boundary-layer interaction, slightly improved velocity profiles are achieved

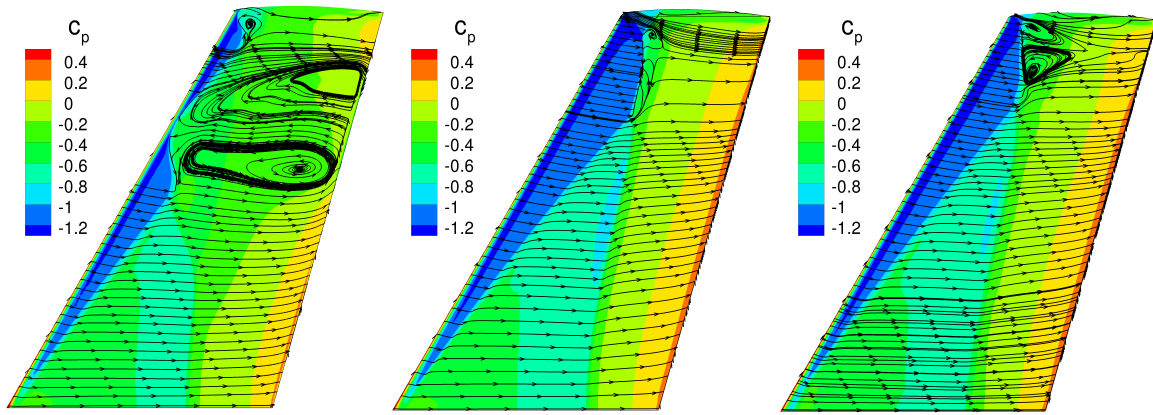


Figure 13. ONERA M6 wing. Surface pressure distribution and friction lines at incidence $\alpha = 4.08^\circ$ predicted by the SST model (left), the SSG/LRR- ω model (middle) and the JHh-v2 model (right).

when using the Reynolds stress models instead of the SST model. The SAO model shows significant deviations of the velocity profiles throughout the whole interaction region. Qualitatively good agreement to experimental results can be found when turbulent stress profiles are compared. Again an improvement of the Reynolds stress models compared to the SST results is obtained.

Moreover an improvement of mean velocity profiles using the Reynolds stress models is observed for the subsonic flow around the HGR-01 airfoil, especially compared to the SAO model. Likewise at airfoil stall the prediction of turbulent shear stresses near the trailing edge is improved.

Considering the transonic flow around the RAE 2822 airfoil, the Reynolds stress models and the SST model predict the shock for Case 9 slightly downstream and for Case 10 slightly upstream of the measured position. These results appear better than the results obtained with the SAO model.

For the ONERA M6 wing the SAO as well as the SST model predict a large shock-induced separation on the outboard wing at an incidence of $\alpha = 4.08^\circ$, leading to a large deviation of the predicted pressure distribution compared to the experiment. In contrast the Reynolds stress models show a much smaller separation zone, leading to a good agreement of the predicted pressure distribution with the measured data, especially for the SSG/LRR- ω model.

References

- ¹Spalart, P. R., Allmaras, S. R., "A one-equation turbulence model for aerodynamic flows" *La Recherche Aérospatiale*, Vol. 1, pp. 5-21, 1994.
- ²Menter, F. R., "Two-Equation Eddy-Viscosity Turbulence Models for Engineering Applications", *AIAA Journal*, Vol. 32 No. 8, pp. 1598-1605, 1994.
- ³Spalart, P. R., Jou, W. H., Strelets, M., Allmaras, S. R., "Comments on the feasibility of LES for wings, and on a hybrid RANS/LES approach", *1st AFOSR International Conference on DNS/LES, Aug. 4-8, 1997, Ruston, LA, Advances in DNS/LES*, edited by C. Liu and Z. Liu, Greyden Press, Columbus, OH, 1997.
- ⁴Menter, F. R., Kuntz, M., and Bender, R. "A scale-adaptive simulation model for turbulent flow prediction", *AIAA paper* 2003-0767, Reno, NV, 2003.
- ⁵Girimaji, S. S., "Partially-Averaged Navier-Stokes Model for Turbulence: A Reynolds-Averaged Navier-Stokes to Direct Numerical Simulation Bridging Approach", *Journal of Applied Mechanics*, Vol. 73 No. 3, pp. 413-421, 2006.
- ⁶Wilcox, D. C., *Turbulence Modeling for CFD*, 2nd. Edition, DCW Industries, La Cañada, CA, 1998.
- ⁷Haase, W., Aupoix, B., Bunge, U., Schwamborn, D., "FLOMANIA – A European Initiative on Flow Physics Modelling", *Notes on Numerical Fluid Mechanics and Multidisciplinary Design*, Vol. 94, Springer, 2006
- ⁸Speziale, C. G., Sarkar, S. Gatski, T. B., "Modelling the pressure-strain correlation of turbulence: an invariant dynamical systems approach", *Journal of Fluid Mechanics*, Vol. 227, pp. 245-272, 1991.
- ⁹Daly, B. J., Harlow, F. H., "Transport equations of turbulence", *Physics of Fluids*, Vol. 13, pp. 2634-2649, 1970.
- ¹⁰Wilcox, D. C., "Reassessment of the Scale-Determining Equation for Advances Turbulence Models", *AIAA Journal*, Vol. 26 No. 11, pp. 1299-1310, 1988.
- ¹¹Launder, B. E., Reece, G. J., and Rodi, W., "Progress in the development of a Reynolds-stress turbulence closure", *Journal of Fluid Mechanics*, Vol. 68, pp. 537-566, 1975.
- ¹²Eisfeld, B. and Brodersen, O., "Advanced Turbulence Modelling and Stress Analysis for the DLR-F6 Configuration", *AIAA paper* 2005-4727, Toronto, Canada, 2005.

- ¹³Jakirlić, S., Hanjalić, K.: “A new approach to modelling near-wall turbulence energy and stress dissipation”, *Journal of Fluid Mechanics*, Vol. 539, pp. 139-166, 2002.
- ¹⁴Probst, A., Radespiel, R.: “Implementation and Extension of a Near-Wall Reynolds-Stress Model for Application to Aerodynamic Flows on Unstructured Meshes”, *AIAA Paper* 2008-770, 2008.
- ¹⁵Lumley, J. L.: “Computational Modeling of Turbulent Flows”, *Adv. Appl. Mech.*, Vol. 18, pp. 123-176, 1978.
- ¹⁶Gibson, M. M. and Launder, B. E.: “Ground Effects on Pressure Fluctuations in the Atmospheric Boundary Layer”, *Journal of Fluid Mechanics*, Vol. 86, pp. 491-511, 1978.
- ¹⁷Schwaborn, D., Gardner, A., von Geyr, H., Krumbein, A., Lüdeke, H., and Stürmer, A., “Development of the TAU-Code for aerospace applications”, *50th NAL International Conference on Aerospace Science and Technology, 2008-06-26 - 2008-06-28, Bangalore, India*, 2008.
- ¹⁸Wieghardt, K., and Tillman, W., “On the Turbulent Friction Layer for Rising Pressure”, NACA TM 1314, 1951.
- ¹⁹Delery, J. and Marvin, J. G. “Shock Wave-Boundary Layer Interactions”, NATO, *AGARDograph* No. 280, 1986.
- ²⁰Dupont, P., Pionniau, S., Sidorenko, A. and Debiève, J. F. “Investigation by Particle Image Velocimetry Measurements of Oblique Shock Reflection with Separation”, *AIAA Journal*, 46(6), 2008.
- ²¹Garnier, E., Sagaut, P. and Deville, M. “Large Eddy Simulation of Shock/Boundary-Layer Interaction”, *AIAA Journal*, Vol. 40 No. 10, pp. 1935-1944, 2002.
- ²²Touber, E. and Sandham, N. D. “Large-eddy simulation of low-frequency unsteadiness in a turbulent shock-induced separation bubble”, *Theor. Comput. Fluid Dyn.*, 23 (2), pp. 79-107, 2009.
- ²³Wokoek, R., Krimmelbein, N., Radespiel, R., Ciobaca, V., Krumbein, A.: “RANS Simulation and Experiments on the Stall Behaviour of an Airfoil with Laminar Separation Bubbles”, *AIAA Paper* 2006-0244, 2006.
- ²⁴Cook, P. H., McDonald, M. A., Firmin, M. C. P., “Aerofoil RAE 2822 – Pressure Distributions, and Boundary Layer and Wake Measurements”, In: J. Barche (Ed.), *Experimental Data Base for Computer Program Assessment*, edited by J. Barche, AGARD-AR-138, Chapter A6, 1979.
- ²⁵“Pressure Distributions on the ONERA-M6-Wing at Transonic Mach Numbers”, edited by J. Barche, AGARD-AR-138, Chapter B1, 1979.